VHF radar images of artificial field-aligned

ionospheric irregularities in the subauroral E region

D. L. Hysell¹, J. Munk², and M.McCarrick³

University, Ithaca, NY, USA

²Electrical Engineering, University of

Alaska Anchorage, Anchorage, AK, USA

³Naval Research Laboratory, Washington,

DC, USA

¹Earth and Atmospheric Sciences, Cornell

Key Points.

- 1. Radar images of *E* region AFAIs generated over HAARP using its twisted-beam mode are presented.
- 2. The spatial distribution of the backscatter is similar but not identical to the HF radiation pattern.
- 3. The most important difference is due to preference for irregularities generated within the Spitze.
- Artificial E-region field-aligned plasma density irregularities (AFAIs) have been
- 4 generated using the HAARP ionospheric modification facility in Gakona and
- observed with a 30-MHz coherent scatter radar imager in Homer, Alaska. The
- 6 AFAIs were generated using a distinctive, twisted-beam antenna pattern that il-
- ⁷ luminated a particularly broad volume overhead. The broad beam facilitates stud-
- $_{8}$ ies of natural sporadic E layer patches when they are present. The center of the
- pattern was pointed at different angles between zenith and magnetic zenith to
- examine the effects on the AFAI morphology. Radar images of AFAIs gener-
- ally resemble the radiation pattern of the HF source, but the irregularities are
- strongest within a narrow range of zenith angles bounded approximately by the
- Spitze angle. A number of factors which might influence AFAI generation and
- detection are examined. The most important is most likely the requirement
- for the pump mode to have a standing-wave component for thermal para-
- metric instability to operate.

1. Introduction

A signature feature of ionospheric modification experiments is the generation of artificial field-aligned plasma density irregularities (AFAIs). The irregularities are generated by thermal parametric instability driven by a strong HF signal propagating upward through the ionosphere. The instability is localized around the upper-hybrid interaction height where the HF pump frequency matches the plasma upper-hybrid frequency. At this height and in the vicinity of nascent plasma density irregularities, linear mode conversion takes place, with the pump HF wave coupling energy into an upper-hybrid wave. Differential 23 wave heating and thermodynamic effects subsequently cause the density irregularities to intensify, signifying instability. Density irregularities take the form of elongated, fieldaligned filaments. Onset occurs when the pump wave amplitude exceeds a threshold value set by relaxation processes. In the nonlinear regime, however, wave trapping occurs in the filaments, the trapped waves are intensified, and the threshold decreases drastically. This is called resonance instability. Electron Bernstein waves play a role if the pump frequency is close to a harmonic of the electron gyrofrequency, complicating the picture. For reviews of thermal parametric instability in the linear and nonlinear regimes, see *Grach* et al. [1978a, b]; Dysthe et al. [1982, 1983]. 32 The AFAIs generated by thermal parametric and resonance instability can be observed with coherent radar backscatter [Inhester et al., 1981; Hedberg et al., 1983; Coster et al., 1985; Hedberg et al., 1986; Hysell et al., 1996; Bond et al., 1997; Hughes et al., 2003; Senior et al., 2004]. The condition for observing them is the same as for naturally-occurring field-aligned irregularities – that the radar wavevector be nearly perpendicular to the back-

ground geomagnetic field. In the high-latitude *F*-region ionosphere, this condition can be
met only when refractive ray bending is significant. AFAIs in the *E* region, meanwhile,
can be observed with much less refraction and accompanying uncertainty in echo location.

Observations of *E*-region AFAIs at VHF frequencies tend to be relatively consistent and
repeatable so long as natural instabilities do not intervene [*Hibberd et al.*, 1983; *Djuth et al.*, 1985; *Nossa et al.*, 2009; *Hysell and Nossa*, 2009]. Conducting such experiments
requires the ability to generate pump HF waves at frequencies below the *E*-region critical
frequency. At present, that capability exists only at HAARP.

This paper describes observations of *E*-region AFAIs generated by the HAARP facility in Gakona, Alaska and observed with a 30-MHz coherent scatter radar imager located approximately 450 km away in Homer, Alaska. We are mainly concerned with studying the spatial configuration of the irregularities in the perpendicular plane. In order to broaden HAARP's radiation pattern, we make use of the "twisted beam" configuration introduced to explore the effects of the orbital angular momentum of the pump signal. Being very broad and relatively uniform, the twisted-beam pattern lends itself to quantitative studies of spatial variations in AFAI generation. Using the twisted beam at HAARP, the modified region moreover becomes larger than the characteristic scale size of some naturally-occurring ionospheric irregularities which are visible to coherent scatter radars during heating experiments. The modified region thereby becomes a canvas on which natural irregularities are painted.

2. Experiment description

- Ionospheric modification experiments were conducted in April, 2014, at the HAARP facility in Gakona, Alaska. The HAARP facility was configured to emit O-mode signals at 2.75 MHz in continuous-wave mode. Pointing was varied every minute across four positions spanning angles between zenith and magnetic zenith. The 12x15 rectangular array of antennas was operated at a full power of 3.6 MW.
- The radiation pattern for HAARP was the so-called "twisted beam" or helical-mode pattern. For any predefined antenna pointing position, the helical mode is formed by adding a progressive phase shift to the emissions from different antennas according to their position on the ground. Whereas conventional beam steering is accomplished through a linear phase progression in a linear direction, the twisted beam comes from a linear phase progression in polar angle measured from the center of the array. The progression must be periodic such that a total shift of $2\pi m$ radians is added for each complete rotation about the center. This implies that there will be destructive interference along the beam boresight; the helical-mode beam has a hole at the middle.
- For these experiments, m=1, and so the mode is termed "OAM+1," where "OAM" denotes orbital angular momentum. Electromagnetic radiation carries both energy and momentum, and the momentum has both linear and angular components [Landau and Lifshitz, 1971]. The linear component is associated with field polarization. The angular component is associated with field spatial distribution and is independent of polarization, i.e., the X and O modes. The phase front of a helical-mode wave is a helix with a pitch that is set by m, the so-called "topological charge," and a handedness that is set by the sign of

m. In the case m=0, the wavefronts revert to planes. All waves with imperfectly planar wavefronts carry nonzero orbital angular momentum.

When radiation interacts with material, it can impart momentum by applying a force in the case of the linear component and a torque in the case of the angular component [*Beth*, 1936]. This makes helical-mode light beams useful in certain kinds of material processing. In telecommunications, helical-mode signals can be used to increase the information-carrying capacity of fixed-bandwidth channels. The exploitation of finite OAM signal components could also be a powerful new tool in radio science [*Thidé et al.*, 2007; *Leyser et al.*, 2009].

For the present application, we are mainly interested in the broad beam afforded by the twisted-beam mode. The solid angle spanned by the beam is inversely proportional to the directivity of the radiation pattern, and the directivity is proportional to the aperture efficiency. The periodic angular phase progression of the antenna array employed for the twisted beam minimizes the directivity and maximizes the beam solid angle. What is more, the uniformity of the twisted beam in the azimuthal direction facilitates a quantitative assessment of the azimuthal distribution of the AFAIs.

Fig. 1 depicts the HAARP radiation pattern for 2.75-MHz emissions using the twisted beam pointed toward zenith (left panel) and magnetic zenith (right panel). The figure accounts for the radiation patterns of the individual elements as well as for the effects of ground. The patterns are squared-off rings with steep east and west sidewalls and deep central depressions. Relatively modest peak directivity is a consequence of low operating frequency and large beamwidth.

The Homer radar is a 30-MHz coherent scatter radar imager deployed atop Diamond Ridge, affording it an unobstructed view of the horizon in the direction of Gakona and HAARP. The radar employs a transmitter producing 12 kW of power with a maximum duty cycle of 7.5% and pulses as long as 200 μ s. For these experiments, 13-bit Barker-coded pulses with a baud width of 1.5 km and an interpulse period of 370 km were used. The radar uses Yagi antenna arrays for transmission and reception which can be phased so that the main beam points precisely in the direction of either Fairbanks or Gakona.

For reception, a software-defined receiver capable of sampling signals from six spaced,
non-colinear antenna groups is used. Matched filtering is implemented digitally. Spectral analysis is typically performed using 64 frequency bins of which only the 16 lowestfrequency bins are retained in this case for analysis. All spectra and cross-spectra are
computed for subsequent analysis. The incoherent integration time for these experiments
is approximately 3 s. The antenna groups used for reception are located so as to form
15 nonredundant interferometry baselines, the longest of which being approximately 15
wavelengths long.

An aperture-synthesis imaging method based on the MaxENT algorithm is used to examine the spatial structure of the backscatter in the plane perpendicular to the geomagnetic
field [Gull and Daniell, 1978; Wilczek and Drapatz, 1985]. The problem is underdetermined and so must be treated using statistical inverse methods. The objective of the MaxENT algorithm is to find the brightness distribution, the distribution of backscatter power
versus bearing, that is congruent with the measured cross-spectral data (within confidence
limits established by error analysis) while maximizing the entropy of the brightness. Shan-

non's entropy is a measure of information content. The image with the highest entropy has 123 the least information, is the most generic, and is most representative of all images consistent with the data. Lower-entropy images are to be rejected, possessing features lacking 125 support in the data. An important attribute of the maximum entropy method is that it does 126 not admit brightness solutions that are anywhere negative and so implicitly rejects an enor-127 mous but inadmissible part of the solution subspace. By some measures, the maximum 128 entropy method is the optimal non-parametric super-resolution imaging method [Kosarev, 1990]. Our algorithm estimates and utilizes the full error covariance matrix and compen-130 sates for the heterogeneous antennas and antenna groups [Hysell and Chau, 2006]. 131

3. Observations

Fig. 2 represents the radar backscatter observed in Homer during the ionospheric modification experiments. Echoes from irregularities over HAARP are the broad patches in
the figure. These echoes are range-aliased such that the actual range is the apparent range
indicated plus 370 km. (Other echoes shown come from specular meteor trails and from
aircraft and are not aliased.)

The rays from Homer to the E region over Gakona are nearly horizontal, and range here is slant range. The modified volume over HAARP consequently spanned almost 80 km in downrange distance. Emissions from HAARP were cycled between one of four zenith angles between zenith and magnetic zenith for one minute each with one-minute heating gaps in between cycles. Corresponding variations in echo range are evident. There was a gradual, secular variation in the nearest range from which echoes were received. The

backscatter intensity varied gradually in time, as did the Doppler shifts. At the very end of the experiment, the AFAIs nearly vanished. The slow secular variations suggest natural changes in the ionosphere over time.

Remarkably, Fig. 2 exhibits quasi-periodic striations with apparent motion away from the radar. The striations are evident in backscatter intensity and also in Doppler shift. They are most evident late in the experiment. Their behavior is not obviously related to the heater cycling and also appears to be indicative of natural ionospheric phenomena. The striations are reminiscent of those analyzed by *Hysell et al.* [2014] and associated with drifting, patchy sporadic *E* layers of the kind commonly found at middle latitudes. Their appearance at subauroral latitudes was novel and constrained the candidate mechanisms that could be responsible.

Because of interference, the ionosonde at HAARP yields no information about the E region when this experiment is running. Prior to the start of the experiment, the ionosonde reported FoE = 3.4 MHz with no indication of sporadic E. After the experiment, the E region was not visible in ionograms. Natural absorption evidently increased during the experiment. We believe patchy sporadic E layers were present at times as well.

Fig. 3 shows four radar images depicting irregularities generated by HAARP pointing in one of four zenith angles between zenith and magnetic zenith. The figures also show contours representing the HAARP radiation pattern, projected to 97 km and corrected for the square of the range. (For the given experimental conditions and on the basis of IRI2016 model runs, we expect the reflection height and the upper-hybrid interaction height to have been approximately 102 km and 97 km, respectively [*Bilitza et al.*, 2016].) The

contours represent directivity in dB relative to the maximum. Dashed curves show the angle between rays from the Homer radar and the local geomagnetic field neglecting the effects of refraction.

Overall, the intensity of coherent backscatter conforms reasonably closely to the HF radiation pattern. In the case of zenith pointing, the backscatter is mainly confined to the
regions within the -3 dB contours. As the zenith angle increases, however, the coherent
scatter imagery departs more significantly from the radiation pattern. In the case of magnetic zenith pointing, the strongest echoes arise from zenith rather than from the regions
where the two HF main beams intersect the ionosphere. The backscatter intensity moreover becomes somewhat asymmetric, with echoes form the rightmost lobe being weaker
than those from the leftmost.

Fig. 4 is similar to Fig. 3 except that it depicts echoes from late in the experiment.

The echoes have become somewhat weaker, most likely due to increased **pump-mode**absorption. Moreover, the echoes in Fig. 4 exhibit considerable structure, particularly on

the northward edges. The echoes are punctuated by periodic striations aligned northwest

to southeast and arrayed northeast to southwest. The wavelength is about 10 km. The

striations have negative Doppler shifts whereas the background backscatter has positive

Doppler shifts. Over time, the striations propagate away from Homer with a period of

As in the previous example, the images in this example indicate a preference for backscatter from the zenith position over HAARP. In the magnetic zenith pointing case,

the echoes from the zenith position are strongest. In this instance, the echoes are approximately symmetric from right to left.

The features depicted in Fig. 4 are similar to those observed by *Hysell et al.* [2014] when 188 a dense, patchy sporadic E layer was present over Gakona. In this case, the twisted-beam 189 mode permits radar imaging over a much broader region of space than what was possible using a standard beam. The features are also similar to sporadic E layers observed with 191 VHF radar imaging in the Caribbean (e.g. [Hysell et al., 2009]). The phenomenology seen here is similar if less common than what occurs at middle latitudes, the difference being 193 that ionospheric modification permits daytime observations which are usually not possi-194 ble otherwise. That the patchy sporadic E layers can occur in the subauroral ionosphere 195 provides important clues about their cause. Specifically, this rules out a role for plasma 196 instabilities which cannot function where the magnetic dip angle is very large.

4. Analysis

Here, we analyze various influences on the coherent backscatter from the AFAIs created over HAARP. The backscatter is not created as if by a searchlight projected on an E-layer screen. Instead, there appears to be a preference for strong echoes near the zenith position over the HF source. Reasons why include HF and VHF propagation effects and, most importantly, the way thermal parametric instability operates in the E region.

4.1. Homer radar beam shape

The Homer radar employs an array of 8 3-element Yagi antennas spaced by 5/8 wavelengths for transmission. Cables introducing a $\lambda/6$ phase progression are used to steer

the beam in the direction of Gakona. The characteristics of the transmitting array control the overall characteristics of two-way radiation pattern. That pattern has a half-power beamwidth of precisely 10° and a beamwidth between first nulls of precisely 20°. In view of the large dynamic range of the echoes registered by the radar, the latter figure is the important one for analyzing the size of the region the radar is capable of imaging. The modified region over HAARP is fully contained within this region. As the Homer radar is on a ridge and has an unobstructed view to Gakona, it is unlikely that the radar itself is influencing the imagery presented here significantly. Indeed, the radar sees aircraft near the horizon over a wider range of azimuths than the AFAIs occupy.

4.2. Pump-mode propagation effects

O-mode radiation emitted from the ground must be able to propagate upward to the altitude where the pump frequency matches the upper-hybrid frequency for thermal parametric instability to operate. Whether it does is governed by the Appleton-Hartree equation which gives the index of refraction for waves propagating in cold magneto-plasmas at a given frequency and direction:

$$n^{2}(\omega,\theta) = 1 - \frac{X}{1 - iZ - \frac{Y^{2}\sin^{2}\theta}{2(1 - X - iZ)} \pm \sqrt{\frac{Y^{4}\sin^{4}\theta}{4(1 - X - iZ)^{2}} + Y^{2}\cos^{2}\theta}}$$
(1)

where $X\equiv\omega_p^2/\omega^2$, $Y\equiv\Omega/\omega$, and $Z\equiv\nu/\omega$ and where the plus and minus signs correspond to the O and X modes, respectively. Here, ω , ω_p , Ω , and ν are the wave, plasma, electron gyro, and electron-neutral collision frequencies, respectively. Ions effects are neglected, and ions just provide a neutralizing background. The angle θ is the angle between the wave vector and the background geomagnetic field.

A simple geometric interpretation described by *Budden* [1985] and attributed to Peover-219 lein can be used to analyze the propagation of waves in a vertically-stratified ionosphere. Consider a vector space spanned by $N_z \equiv n \cos \theta'$ and $N_x \equiv n \sin \theta'$ where θ' is the zenith 221 angle in the magnetic meridian, \hat{z} is the vertical direction, and \hat{x} is horizontal and perpen-222 dicular to the magnetic field. Fig. 5 shows index of refraction surfaces for five values of 223 X and for Y = 0.5 plotted in that space. For the figure, the magnetic dip angle was taken 224 to be $\chi = 14^{\circ}$. According to Snell's law, waves will propagate along vertical lines in this space with N_x given by the sine of the zenith angle at ground level θ'_{\circ} . As the wave prop-226 agates, the ray normal direction will be everywhere parallel to the outward unit normal of 227 the index of refraction surfaces [Budden, 1985]. 228

For a wave to reach the reflection height, the vertical line must pass through the corresponding index of refraction surface (X=1, the Spitze). According to Eq. 1, the condition for reflection is $\sin(\theta_{\circ}') \leq \sqrt{\frac{Y}{1+Y}} \sin \chi$. For our experiments, $Y\approx 0.54$, and the Spitze angle is approximately 8.26° .

More directly relevant here is the range of angles within which O-mode waves launched from the ground reach the upper-hybrid interaction height where $X=1-Y^2$. This is a less restrictive condition. Nossa et al. [2009] evaluated this condition numerically for conditions relevant to the current experiment. However, their calculations considered only angles in the plane of the magnetic meridian. To generalize the problem to three dimensions, we must generalize the geometric construction in Fig 5, regarding the ellipses as ellipsoids in a 3-D space including also $N_x=n\sin\theta\cos\phi$ and $N_y=n\sin\theta\sin\phi$, ϕ being the azimuthal direction in local magnetic coordinates.

Fig. 6 shows the maximum zenith angle for which O-mode waves will reach the upperhybrid interaction height as a function of azimuth angle for three different values of Y. The figure was computed for a magnetic declination angle of 19° which is relevant here. The lower the pump frequency, the larger the region where the condition can be satisfied. The region is slightly elongated in the direction of the magnetic meridian. It is considerably larger than the region enclosed by the Spitze.

Most importantly, the region is considerably larger than the region occupied by AFAIs generated over HAARP. It is unlikely that constraints on the ability of HF pump waves to propagate to the upper-hybrid interaction height significantly influence the radar imagery presented in Figs. 3 and 4.

4.3. VHF propagation effects

Figs. 3 and 4 show the angles between rays from Homer and the geomagnetic field in the scattering region over Gakona. The angles are mainly between $92-93^{\circ}$. As we expect the irregularities in question to be highly field aligned, some refractive ray bending is evidently required to observe them with coherent scatter. Generally, if there is enough E region ionization to satisfy the conditions for AFAI generation, there is enough ray bending for coherent scatter to be seen. This is shown below with the help of ray tracing.

We have implemented an updated version of the raytracing code described by *Jones and*Stephenson [1975], incorporating a more efficient ordinary differential equation solver

based on Ames multistep method [Shampine and Gordon, 1975]. The code considers

plasma number densities from the IRI-2016 model and the magnetic field geometry speci
fied by IGRF for the given date, time, and conditions [Bilitza et al., 2016; Thébault et al.,

²⁶² 2015]. Electron-neutral collisions are also considered. The code is used here to determine the altitudes where the condition for field-aligned backscatter are met.

Fig. 7 shows raytracing calculations for the current experiment. The panel on the left

indicates the altitudes where rays from Homer are perpendicular to the geomagnetic field. 265 The panel on the right indicates how far in degrees the rays depart from perpendicular 266 propagation at an altitude of 97 km. Comparison with the contours in Figs 3 and 4 demon-267 strates how refraction affects the scattering geometry for 30-MHz coherent backscatter. In the E-region scattering volume over Gakona, the angles between the rays from Homer 269 and the geomagnetic field are mainly less than 1°. The angles are somewhat larger in volumes to the south, reaching about 1.2° in the direction of magnetic zenith. The condition 271 for field-aligned backscatter is therefore more closely satisfied at zenith than at magnetic 272 zenith although the difference is less dramatic when the effects of refraction are considered. 273 We might expect natural, intermediate-scale irregularities associated with sporadic E to 274 expand the region where the condition for field-aligned backscatter to be satisfied. Images of patchy sporadic E layers shown by Hysell et al. [2014] contained backscatter from 276 AFAIs outside the main beam of the HAARP antenna pattern. In the case of Fig. 4, however, the scattering zone did not increase significantly when E_s-layer irregularities ap-278 peared. The condition for field-aligned backscatter does not appear to have been a limiting factor in the present experiments. 280

4.4. Threshold for thermal parametric instability

Another, potentially more important geometric effect involves the role played by HF pump-mode reflection in thermal parametric instability. In the vicinity of plasma density

264

irregularities, the HF pump mode induces transverse (to B) polarization electric fields. The
amplitude of the fields is greatest near the upper-hybrid resonance height where the longitudinal projection of the dielectric tensor for upper-hybrid waves nearly vanishes. The polarization electric field combines with the pump-mode field in heating the electrons. Thermal
forcing subsequently modifies the plasma density, accentuating the original plasma density
irregularity and leading to instability. In the nonlinear regime, wave trapping concentrates
the heating, leading to more robust resonance instability.

Just above and below the upper-hybrid resonance resonance, the sign of the longitudinal 290 projection of the dielectric tensor is different, and the directions of the induced polarization electric fields are reversed. To first order, a heating enhancement on one side of the 292 resonance height will be offset by an equal heating deficit on the other side. As the ther-293 mal conductivity in the parallel (to B) direction is very high, one might expect the effects 294 to cancel, negating the instability Das and Fejer [1979]. Dysthe et al. [1983] argue that the symmetry is broken mainly by the Airy pattern associated with pump-mode reflection [Thidé and Lundborg, 1986]. The pump amplitude will necessarily be different above and 297 below the upper-hybrid resonance height, preventing the aforementioned cancellation and restoring instability. 299

In the context of E-region heating, non-resonant electron-neutral collisions widen the upper-hybrid resonance which can span a significant fraction of the pump-mode wavelength [$Hysell\ et\ al.$, 2010]. Even so, the modulating effect of the Airy pattern is sufficient to break the symmetry and allow thermal parametric and resonance instability to occur. The predicted and measured instability threshold for pump-mode amplitude agree closely.

The condition for reflection is only met for pump-mode radiation falling within the
Spitze angle. Outside the Spitze, pump-mode waves are traveling waves. In view of
the preceding discussion, thermal parametric instability should be most robust near zenith
within the region defined by the Spitze angle. This would seem to be a more important
constraint on the echo morphology seen in Figs. 3 and 4 than the other factors analyzed
here. Quantifying the effect is rather difficult, however, as the full-wave theory for radio
waves propagating in the ionosphere off zenith remains not very well developed.

5. Summary and Conclusions

Artificial field-aligned plasma density irregularities have been generated in the *E*-region ionosphere over the HAARP facility and detected with a VHF coherent scatter radar imager in Homer, Alaska. The AFAIs were generated using a twisted-beam mode at HAARP. The twisted-beam mode was chosen for its very broad beam which is relatively uniform and nearly azimuthally symmetric. This facilitates quantitative assessment of spatial variations in AFAI generation. Antenna pointing was varied to assess the effects on the morphology of the modified volume.

Toward the end of the experiment, natural, intermediate-scale irregularities indicative of a patchy E_s layer emerged in the modified volume. Patchy E_s layers normally cannot be observed with coherent scatter during the day. Strong, natural meter-scale irregularities occur seldom or not at all in the daytime when the E region background conductivity is high. Ionospheric modification provides a means of observing E_s layers under a broad

range of background conditions. The twisted-beam mode illuminates a region of space large enough to include several patches and waveforms.

The imaging experiments reveal a bias for AFAIs created near zenith in a range of zenith 326 angles bound approximately by the Spitze angle. The bias does not appear to be a conse-327 quence of the VHF radar radiation pattern. Nor is it defined by the range of zenith angles 328 across which HF pump-mode rays can propagate to the upper-hybrid interaction region. In 329 our experiments, the condition for field-aligned backscatter is met somewhat more closely in the zenith position over HAARP than in the magnetic-zenith position. While we have 331 not independently estimated the magnetic aspect sensitivity of AFAIs, we do not believe 332 this to be a crucial factor in the present experiments. Before being in Homer, Alaska, the 333 30-MHz radar was deployed in Seldovia, about 22 km to the south [Hysell, 2008]. The ge-334 ometry from Seldovia was such that the locus of perpendicularity for E-region backscatter 335 was precisely at zenith over Gakona. AFAI echo characteristics observed from Seldovia 336 were not appreciably different, however.

An important requirement for heater-induced thermal parametric instability is inhomogeneity in the pump-mode signal. As described by *Dysthe et al.* [1983], inhomogeneity is required to break the symmetry above and below the upper-hybrid resonance height that would otherwise defeat instability at high latitudes where the magnetic field lines are nearly vertical. The Airy pattern associated with reflection is the most obvious and important source of inhomogeneity. The threshold calculations made by *Dysthe et al.* [1983] assumed vertical-incidence pump-mode waves and were based on local rather than full-wave theory. While we do not have a full-wave theory for off-vertical incidence, it is

- reasonable to assume that inhomogeneity should be weaker outside the Spitze. In order to
- test the idea, we can perform more experiments in the future, including pointing positions
- further away from magnetic zenith and closer to the locus of perpendicularity.
- Acknowledgments. This research was supported by awards AGS-1342895 and AGS-
- 1634014 from the National Science Foundation to Cornell University. Data used for this
- publication are available through the Madrigal database at http://www.openmadrigal.org.

References

- Beth, R. A., Mechanical detection and measurement of the angular momentum of light,
- ³⁵³ *Phys. Rev.*, 50, 115–125, 1936.
- Bilitza, D., D. Altadill, B. Reinisch, I. Galkin, V. Shubin, and V. Truhlik, The International
- Reference Ionosphere: Model Update 2016, in EGU General Assembly Conference Ab-
- stracts, vol. 18, p. 9671, 2016.
- Bond, G. E., T. R. Robinson, P. Eglitis, D. Wright, A. Stocker, M. Rietveld, and T. Jones,
- Spatial observations by the CUTLASS coherent scatter radar of ionospheric modification
- by high power radio waves, *Ann. Geophys.*, 15, 1412–1421, 1997.
- Budden, K. G., *The Propagation of Radio Waves*, Cambridge Univ. Press, New York, 1985.
- Coster, A. J., F. T. Djuth, R. J. Jost, and W. E. Gordon, The temporal evolution of 3-m
- striations in the modified ionosphere, *J. Geophys. Res.*, 90, 2807–2818, 1985.
- Das, A. C., and J. A. Fejer, Resonance instability of small-scale field-aligned irregularities,
- *J. Geophys. Res.*, 84, 6701–6704, 1979.

- Djuth, F. T., et al., Observations of E region irregularities generated at auroral latitudes by
- a high-power radio wave, *J. Geophys. Res.*, 90, 12,293–13,206, 1985.
- Dysthe, K., E. Mjølhus, H. Pécseli, and K. Rypdal, Thermal cavitons, *Phys. Scr. T.*, 2,
- 548–559, 1982.
- Dysthe, K., E. Mjølhus, H. Pécseli, and K. Rypdal, A thermal oscillating two-stream insta-
- bility, *Phys. Fluids*, 26, 146, 1983.
- Grach, S. M., A. N. Karashtin, N. A. Mityzkov, V. O. Rapoport, and V. Y. Trakhtengerts,
- Theory of thermal parametric instability in an inhomogenous plasma, Sov. J. Plasma
- ³⁷³ *Phys.* (Engl. Transl.), 4, 737–741, 1978a.
- Grach, S. M., A. N. Karashtin, N. A. Mityzkov, V. O. Rapoport, and V. Y. Trakhtengerts,
- Theory of thermal parametric instability in an inhomogenous plasma (nonlinear theory),
- 376 Sov. J. Plasma Phys. (Engl. Trans.), 4, 742–747, 1978b.
- Gull, S. F., and G. J. Daniell, Image reconstruction from incomplete and noisy data, *Nature*,
- 272, 686, 1978.
- Hedberg, Å., H. Derblom, and B. Thidé, Observations of HF backscatter associated with
- the heating experiment at Tromsø, *Radio Sci.*, 18, 840–850, 1983.
- Hedberg, Å., H. Derblom, G. Hamberg, B. Thidé, H. Kopka, and P. Stubbe, Measurements
- of HF backscatter cross section for striations created by ionospheric heating at different
- power levels, *Radio Sci.*, 21, 117–125, 1986.
- Hibberd, F. H., E. Nielsen, P. Stubbe, H. Kopka, and M. T. Rietveld, Production of auroral
- zone E region irregularities by powerful HF heating, J. Geophys. Res., 88, 6347–6351,
- 1983.

- Hughes, J. M., W. A. Bristow, R. T. Parries, and E. Lundell, SuperDARN observa-
- tions of ionospheric heater-induced upper hybrid waves, Geophys. Res. Lett., 30(24),
- doi:10.1029/2003GL018,772, 2003.
- Hysell, D. L., 30 MHz radar observations of artificial E region field-aligned plasma irreg-
- ³⁹¹ ularities, *Ann. Geophys.*, 26, 117–129, 2008.
- Hysell, D. L., and J. L. Chau, Optimal aperture synthesis radar imaging, *Radio Sci.*, 41,
- 10.1029/2005RS003,383, RS2003, 2006.
- Hysell, D. L., and E. Nossa, Artificial *E* region field-aligned plasma irregularities generated
- at pump frequencies near the second electron gyroharmonic, Ann. Geophys., 27, 2711–
- ³⁹⁶ 2720, 2009.
- Hysell, D. L., M. C. Kelley, Y. M. Yampolski, V. S. Beley, A. V. Koloskov, P. V. Pono-
- marenko, and O. F. Tyrnov, HF radar observations of decaying artificial field aligned
- irregularities, *J. Geophys. Res.*, 101, 26,981, 1996.
- 400 Hysell, D. L., E. Nossa, M. F. Larsen, J. Munro, M. P. Sulzer, N. Aponte, and S. A.
- González, Sporadic E layer observations over Arecibo using coherent and incoherent
- scatter radar: Assessing dynamic stability in the lower thermosphere, J. Geophys. Res.,
- 403 114, A12303, doi:10.1029/2009JA014,403, 2009.
- 404 Hysell, D. L., E. Nossa, and M. McCarrick, Excitation threshold and gyroharmonic sup-
- pression of artificial E region field-aligned plasma density irregularities, Radio Sci.,
- 406 RS6003, doi: 10.1029/2010RS004,360, 2010.
- 407 Hysell, D. L., J. Munk, and M. McCarrick, Sporadic E ionization layers ob-
- served with radar imaging and ionospheric modification, Geophys. Res. Lett., 41,

- DOI:10.1002/2014GL061,691, 2014.
- Inhester, B., A. C. Das, and J. A. Fejer, Generation of small-scale field-aligned irregulari-
- ties in ionospheric heating experiments, J. Geophys. Res., 86, 9101–9105, 1981.
- Jones, R. M., and J. J. Stephenson, A versatile three-dimensional ray tracing computer
- program for radio waves in the ionosphere, *Tech. Rep.* 75-76, U. S. Department of Com-
- merce, 1975.
- Kosarev, E. L., Shannon's superresolution limit for signal recovery, *Inverse Problems*, 6,
- 416 55–76, 1990.
- Landau, L. D., and E. M. Lifshitz, *The Classical Theory of Fields, 3rd ed.*, Pergamon Press,
- New York, 1971.
- Leyser, T. B., L. Norin, M. McCarrick, T. R. Pedersen, and B. Gustavsson, Radio pumping
- of ionospheric plasma with orbital angular momentum, *Phys. Rev. Lett.*, 102, 2009.
- Nossa, E., D. L. Hysell, C. T. Fallen, and B. J. Watkins, Radar observations of artificial
- E-region field-aligned irregularities, Ann. Geophys., 27, 2699–2719, 2009.
- Senior, A., N. D. Borisov, M. J. Kosch, T. K. Yeoman, F. Honary, and M. T. Rietveld, Milti-
- frequency HF radar measurements of artificial F-region field-aligned irregularities, Ann.
- *Geophys.*, 22, 3503–3511, 2004.
- Shampine, L. F., and M. K. Gordon, Computer solution of ordinary differential equations,
- The initial value problem, Freeman and Co., San Francisco, 1975.
- Thébault, E., et al., International geomagnetic reference field: the 12th generation, *Earth*,
- *Plantes, and Space, 67, DOI: 10.1186/s40,623–015–0228–9, 2015.*

- Thidé, B., and B. Lundborg, Structure of HF pump in ionospheric modification experi-
- ments, *Physica Scripta*, *33*, 475–479, 1986.
- Thidé, B., H. Then, J. Sjöholm, K. Palmer, J. E. S. Bergman, T. D. Carozzi, Y. N. Istomin,
- N. H. Ibragimov, and R. Khamitova, Utlilization of photon orbital angular momentum
- in the low-frequency radio domain, *Phys. Rev. Lett.*, 99, 087,701, 2007.
- Wilczek, R., and S. Drapatz, A high accuracy algorithm for maximum entropy image
- restoration in the case of small data sets, *Astron. Astrophys.*, 142, 9, 1985.

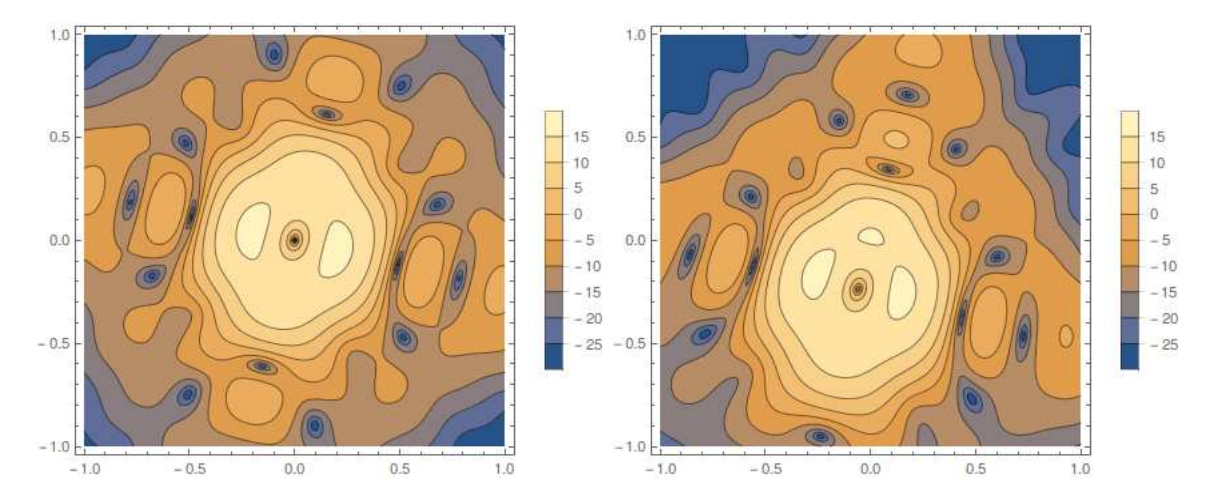


Figure 1. Radiation pattern for the twisted-beam directed toward zenith (left panel) and magnetic zenith (right panel). The horizontal and vertical axes are the direction cosines with respect to east and north, respectively. The legend indicates directivity in dB. The figures were computed for 2.75-MHz emissions.

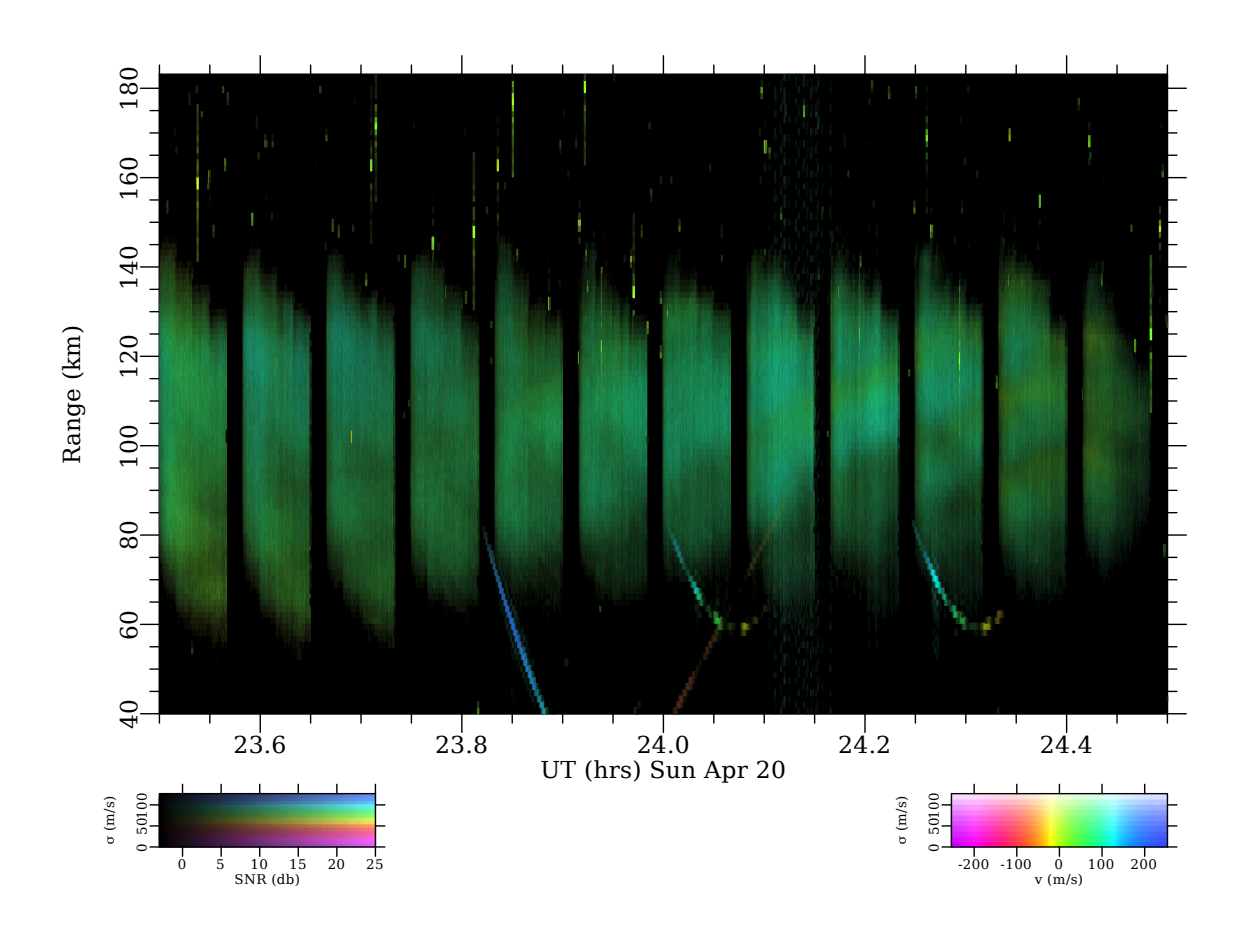


Figure 2. Range-time-Doppler-intensity (RTDI) representation of radar backscatter observed with the Homer radar. The brightness, hue, and saturation of the pixels in the image reflect the signal-to-noise ratio, Doppler shift, and spectral width of the echoes according to the legend shown. Note that UT = LT + 4 hr.

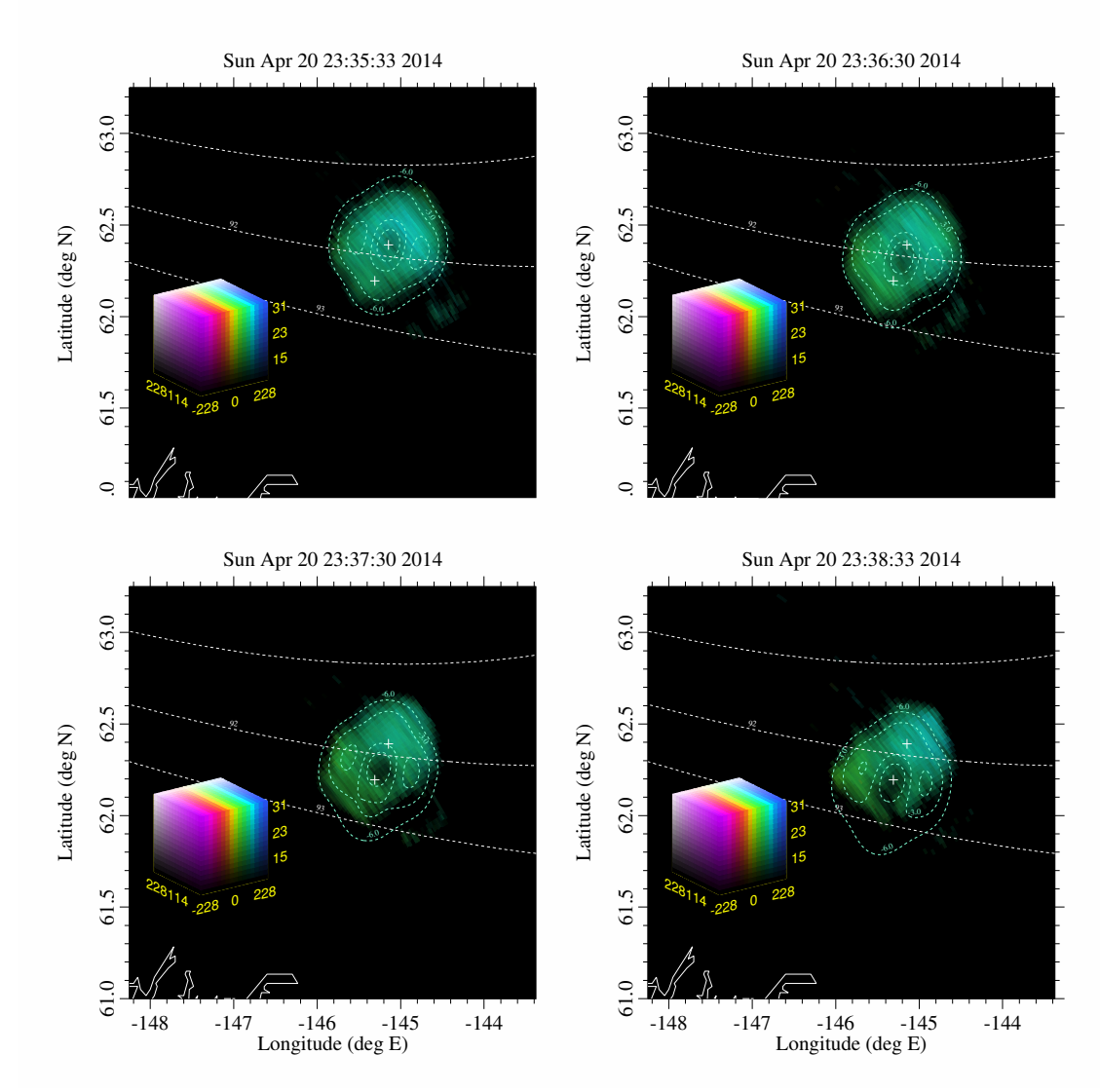


Figure 3. Radar images of the modified volume over HAARP at four times representing four different beam pointing directions (upper-left: 0°, upper right: 4.7°, lower left: 9.3°, lower right: 14°). The brightness, hue, and saturation of the pixels represent echo signal-to-noise ratio, Doppler shift, and spectral width according to the legend shown. Dashed contours represent the HAARP radiation pattern projected to an altitude of 97 km and corrected for the square of the range. (The contours are at the -1, -3, and -6 dB levels.) Dashed lines are the angle between rays from the Homer radar and the geomagnetic field, neglecting refraction.

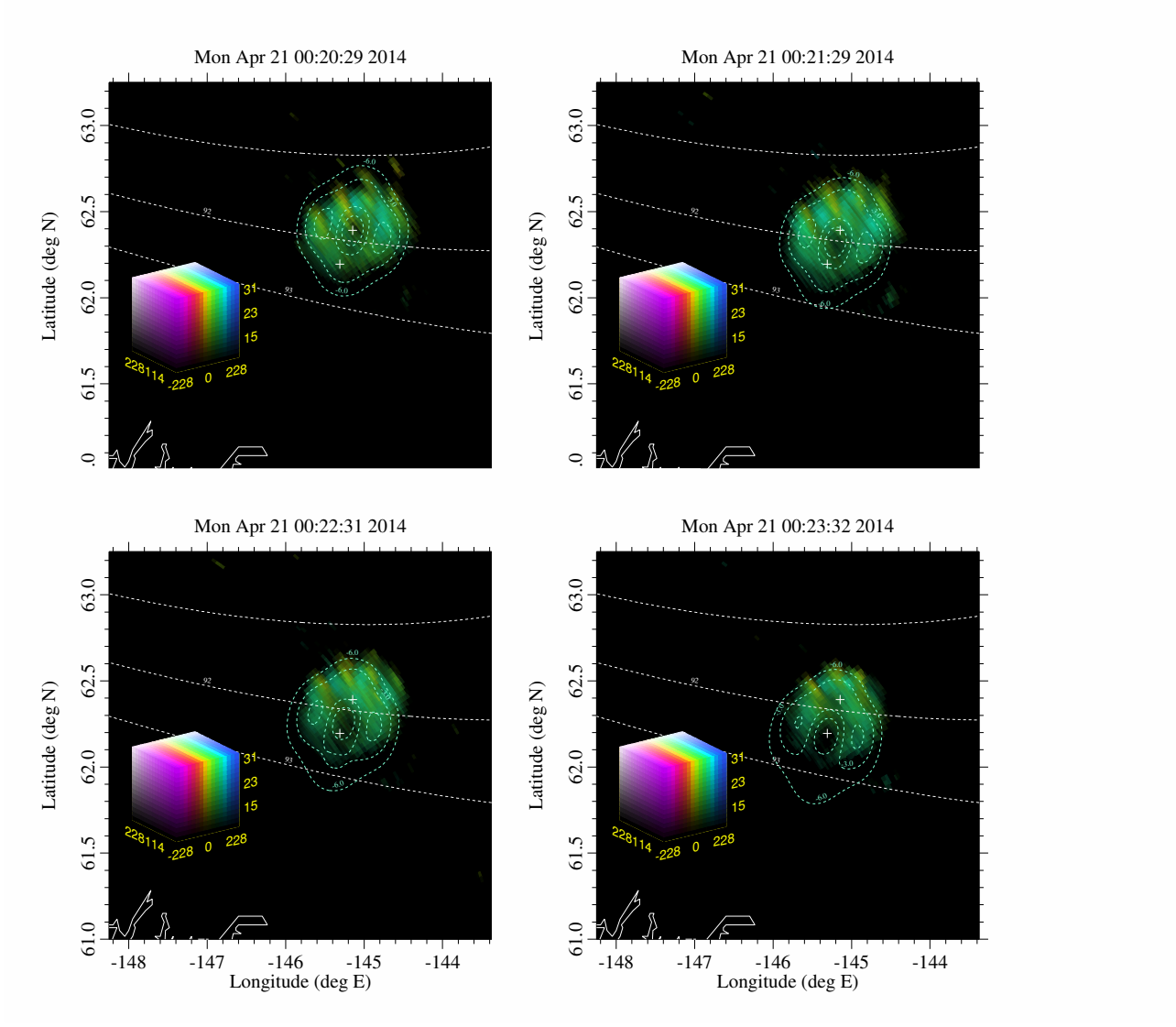


Figure 4. Same as Fig. 3 except when natural background irregularities were also present.

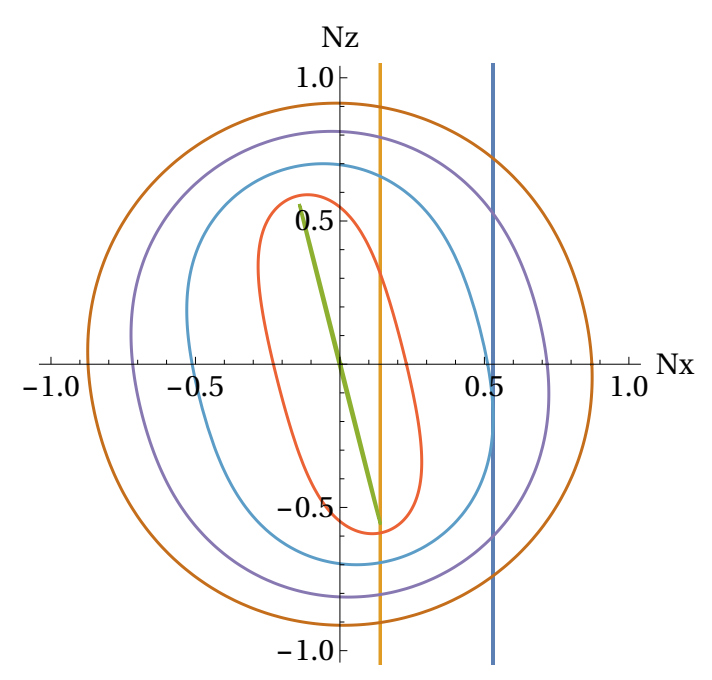


Figure 5. Index of refraction surfaces for (from outside to inside) X = 1, 0.95, 0.5, 0.25,and 0 given Y = 0.5. Vertical lines depict two propagating wave solutions (see text).

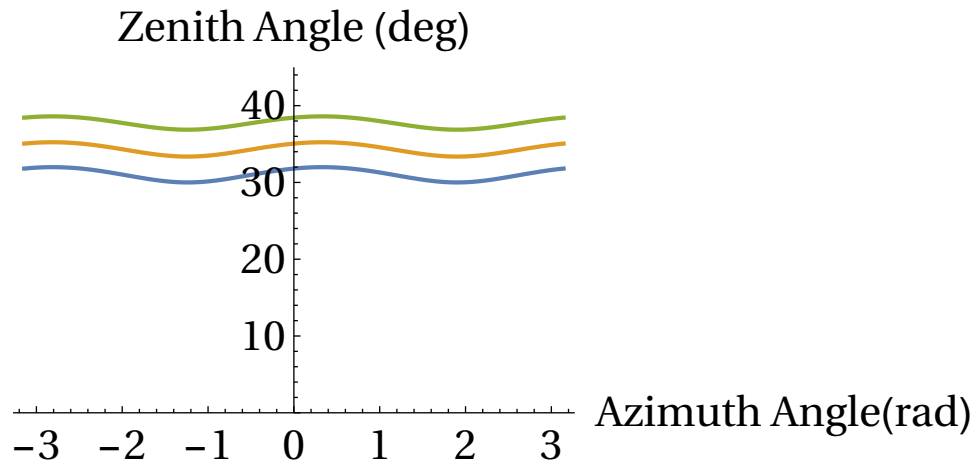


Figure 6. Maximum zenith angles for which O-mode waves can propagate to the upperhybrid interaction height. The three curves reflect results for Y = 0.5 (blue) 0.55 (orange), and 0.6 (green). Azimuth angle is measured clockwise from true north.

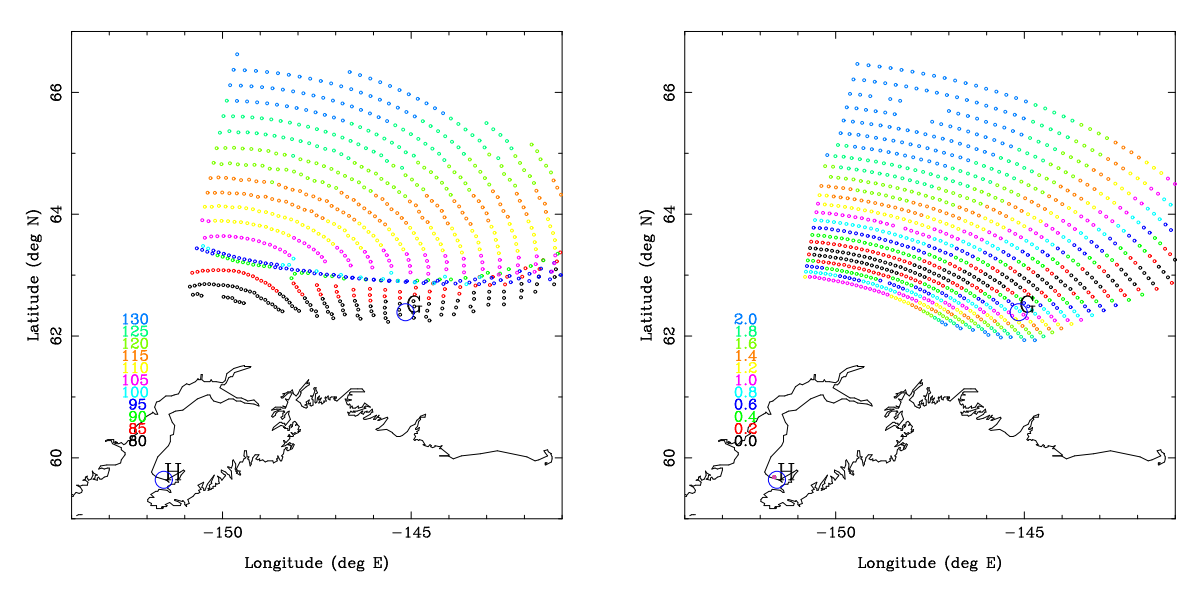


Figure 7. Results of raytracing calculations for the radar signals from Homer. (left panel) Altitudes where the rays are normal to the geomagnetic field. (right panel) Angular departure from normality, in degrees, for rays at 97-km altitude. "G" and "H" designate Gakona and Homer, respectively. The blue circle near Gakona is centered on zenith and has a radius that intercepts magnetic zenith. The condition for field-aligned backscatter is nearly but not perfectly satisfied within the circle.